Nanoscale organization of nicotinic acetylcholine receptors revealed by stimulated emission depletion microscopy

R.R. Kellner, C.J. Baier, Katrin Willig, S.W. Hell, F.J. Barrantes

Angaben zur Veröffentlichung / Publication details:

Kellner, R.R., C.J. Baier, Katrin Willig, S.W. Hell, and F.J. Barrantes. 2007. "Nanoscale organization of nicotinic acetylcholine receptors revealed by stimulated emission depletion microscopy." *Neuroscience* 144 (1): 135–43. https://doi.org/10.1016/j.neuroscience.2006.08.071.

NANOSCALE ORGANIZATION OF NICOTINIC ACETYLCHOLINE RECEPTORS REVEALED BY STIMULATED EMISSION DEPLETION MICROSCOPY

R. R. KELLNER,[a] C. J. BAIER,[b] K. I. WILLIG,[a] S. W. HELL[a]* AND F. J. BARRANTES[b]

[a]*Max Planck Institute for Biophysical Chemistry, Department of NanoBiophotonics, 37077 Göttingen, Germany*

[b]*UNESCO Chair of Biophysics & Molecular Neurobiology and Instituto de Investigaciones Bioquímicas, 8000 Bahía Blanca, Argentina*

Fast synaptic transmission as mediated by the neurotransmitter acetylcholine imposes concentration and spatial requirements to achieve high efficacy. The high density of nicotinic acetylcholine receptors (AChRs), tightly aggregated in the form of micron-sized two-dimensional clusters, is a characteristic feature of the postsynaptic membrane of innervated adult neuromuscular junctions (NMJ) (Sanes and Lichtman, 2001). Postsynaptic maturation can occur, and clusters form, in the absence of nerve (Kummer et al., 2004), but it is not known how these supramolecular aggregates are constructed at the cell surface in the absence of innervation (Willmann and Fuhrer, 2002; Sanes and Lichtman, 2001). Before establishment of these postsynaptic specializations, AChRs shift from a diffusely dispersed to a submicron-sized cluster distribution during the early stages of embryonic development of the NMJ (Willmann and Fuhrer, 2002; Sanes and Lichtman, 2001). These marked changes in AChR supramolecular organization occur within a very narrow time window in ontogeny, between embryonic stages E13 and E14 (Sanes and Lichtman, 2001).

Due to their diffraction-limited resolving power, epifluorescence and confocal microscopes fall short of resolving the fine structure of these small clusters. However, recent advances in physical optics have shown that the diffraction limit of far-field fluorescence microscopy can be overcome by applying the principles of stimulated emission depletion (STED) (Hell and Wichmann, 1994; Klar et al., 2000; reviewed in Hell, 2003). STED is a member of a new family of microscopy concepts that, despite using regular lenses, entails diffraction-unlimited resolution (Hell, 1997, 2004). In STED microscopy the excitation beam is overlapped with a second, red-shifted doughnut-shaped beam that de-excites fluorophores by stimulated emission. Spatial and temporal alignment of the excitation focal spot with the de-exciting beam ensures that fluorescence originates only from the central area of the excitation spot where the power of the doughnut beam is close to zero (Supplementary Fig. S1). By increasing the intensity of the de-exciting beam beyond a saturation threshold, the resulting fluorescent spot of the STED microscope can be narrowed down to the molecular scale (Hell, 1997, 2003).

Here we apply STED microscopy to visualize the organization of AChR supramolecular aggregates below the diffraction resolution limit. To this end cell-surface AChRs were studied in CHO-K1/A5 cells, a heterologous mammalian cell expression system obtained in one of our laboratories. CHO-K1/A5 is a clonal cell line stably expressing substantial amounts of adult murine AChR devoid of non-receptor anchoring proteins (Roccamo et al., 1999), and thus constituting an excellent model system to study the distribution and organization of this cell-surface receptor.

*Corresponding author. Tel: +49-551-2012501; fax: +49-551-2012505. E-mail address: hell@nanoscopy.de (S. W. Hell).

Abbreviations: AChR, nicotinic acetylcholine receptor; □BTX, □ bungarotoxin; CDx, methyl-□-cyclodextrin; CI, confidence interval; CSR, complete spatial randomness; fix–label, fixation followed by labeling; FWHM, full-width-half-maximum; label–fix, labeling followed by fixation; NMJ, neuromuscular junction; STED, stimulated emission depletion; TMA-DPH, 1-(4-trimethylammoniumphenyl)-6-phenyl-1,3,5-hexatriene *p*-toluenesulfonate.

EXPERIMENTAL PROCEDURES

Cell culture

CHO-K1/A5 cells were grown in Ham's F12 medium supplemented with 10% fetal bovine serum (FBS) for 2–3 days at 37 °C as in Roccamo et al. (1999) before cytochemical experiments.

Preparation of single plasma membrane sheets

For preparation of membrane sheets, CHO-K1/A5 cells were grown on polylysine-coated glass coverslips and disrupted as described by Avery et al. (2000) using a 300 ms ultrasound-pulse in ice-cold KGlu buffer (20 mM Hepes, pH 7.2, containing 120 mM potassium glutamate and 20 mM potassium acetate).

Cholesterol depletion of cells and single plasma membrane sheets

CHO-K1/A5 cells and plasma membrane sheets, on the same coverslips, were treated with 10 mM methyl-□-cyclodextrin (CDx; Sigma Chemical Co., St. Louis, MO, USA) in KGlu-buffer for 20 min at 37 °C to deplete their cholesterol content.

Fluorescence labeling

In order to stain only cell-surface AChRs, CHO-K1/A5 cells were labeled with fluorescent Alexa^{594}-□-bungarotoxin (□BTX) (Molecular Probes, Eugene, OR, USA) or with the monoclonal anti-AChR antibody mAb210 (Sigma Chemical Co.), followed by staining with secondary antibodies previously conjugated to the dye Atto 532. The latter fluorochrome (provided by K. H. Drexhage, Chemistry Department, University of Siegen, Siegen, Germany) was coupled to an affinity purified sheep anti-mouse IgG (Jackson ImmunoResearch Laboratories, West Grove, PA, USA) via its succinimidyl ester.

In the □BTX staining procedure, cells and membrane sheets were stained with Alexa^{594}-□BTX for 1 h at 4 °C in KGlu buffer containing 1% BSA. In the antibody staining procedure, cells and membrane sheets were incubated with mAb210 for 1 h at 4 °C, repeatedly washed, and labeled with sheep anti-mouse conjugated with the green-emitting dye Atto 532 for 1 h at 4 °C. When using antibodies, three different conditions were employed: In the "fix-label" condition, samples were fixed with 4% paraformaldehyde before labeling, in order to avoid AChR crosslinking (Tzartos et al., 1987). Secondly, in the "label-fix" condition, fixation followed labeling to allow for antibody-induced AChR patching. Thirdly, when the effect of cholesterol depletion was studied ("CDx-label-fix"), samples were treated with CDx and stained with antibodies as described above and fixed. Finally samples were mounted in Mowiol (6 g Glycerol AR (#4094, Merck, Darmstadt, Germany), 2.4 g Mowiol 4–88 (Hoechst, Frankfurt, Germany), 6 ml water, 12 ml 0.2 M Tris buffer, pH 7.2) and imaged.

Wide-field fluorescence microscopy

Images of whole cells and single membrane sheets obtained by ultrasound treatment (see below) were obtained using conventional epifluorescence microscopy. In some experiments imaging was first undertaken in PBS containing 25 □l/ml of a saturated 1-(4-trimethylammoniumphenyl)-6-phenyl-1,3,5-hexatriene *p*-toluenesulfonate (TMA-DPH) solution (Molecular Probes) in PBS. TMA-DPH allows one to visualize the lipid moiety of membranes and thus facilitate the identification of the ultrathin membrane sheets using a Nikon E-300 fluorescence microscope with a 100×1.4 N.A. oil immersion objective driven by a piezoelectric nanopositioning system (PI Instruments GmbH, Karlsruhe, Germany). Imaging was accomplished with Hamamatsu Orca camera driven by MetaMorph 5.0 software. Appropriate dichroic and emission filters were employed to avoid crossover of fluorescence emission.

STED microscopy

Dyes were excited with a laser diode (Picoquant, Berlin, Germany) emitting 100 ps pulses at 490 nm wavelength. The diode was triggered by the STED pulses delivered by an optical parametric oscillator (OPO, APE, Berlin, Germany), which was synchronously pumped by a Ti:Sapphire laser (MaiTai, Spectra Physics, Mountain View, CA, USA) operating at 80 MHz. The STED pulses with a wavelength of 615 nm were stretched to 200 ps by dispersion in a glass fiber and converted into a focal doughnut by means of a spatial light modulator (Hamamatsu, Hamamatsu City, Japan) delivering a helical phase ramp (0–2□). Using custom-designed dichroic mirrors both beams were coupled into an oil immersion lens (HCX PL APO, 100×, Leica Microsystems, Mannheim, Germany). The typical average power of the excitation and the STED beam at the sample was 2 □W and 14 mW, respectively. The fluorescence collected by the lens was imaged onto a counting avalanche photodiode, with an opening diameter of 71% of that of the back-projected fluorescence spot. STED-imaging was obtained by piezo-scanning the sample at a pixel dwell time of ~0.3 ms with a pixel spacing of 15 nm×15 nm. The effective point spread function of this system was determined experimentally by imaging glass-adsorbed, point-like primary antibodies stained with Atto532 labeled secondary antibodies. Lorentzian fits on the intensity profiles revealed a full-width-half-maximum (FWHM) of 70.8±2.3 nm (mean±S.E.M., data not shown), which is approximately the lateral resolution of this setup.

Data analysis

Brightness and FWHM of individual AChR nanoclusters were evaluated with macros written in MatLab (The Mathworks Inc., Natick, MA, USA) in 7.5×7.5 □m^2 images having a pixel spacing of 15 nm×15 nm. The user interactively defines a region enclosing the dot of fluorescence in the image (see Fig. S2 in supplementary material). The background level and the FWHM of the focal spots in the x- and y-direction were derived from Lorentzian fits. The brightness was defined as the background corrected sum over all pixels within the FWHM. Averages of the values for the dots in the x- and y-directions were retained for each dot and exported for statistical analysis. To ensure that FWHM measurements were not affected by dots that were close together, a stringent chi^2 cutoff of less than a 0.02 difference between the fit and the data was placed on the Lorentzian fit to the dots. See also Supplementary Fig. S2. Histograms of the FWHM and brightness (mean±S.D.) for different experimental conditions are illustrated in Fig. 3 and Fig. S3. The actual size of AChR nanoclusters was estimated by means of deconvolution with the effective point spread function in the STED mode.

For a quantitative analysis of the distribution of spatial point patterns, Ripley's K-test (Ripley, 1977, 1979) was incorporated. In particular, this method allows comparison of observed spatial point patterns with patterns of complete spatial randomness (CSR) on various length scales by taking into account the distances between all points in an area of interest. The expected number of neighbors $N(r)$ for each individual particle within the distance r is characterized by Ripley's K-function: $N(r) = \rho K(r)$, where ρ denotes the particle density of N individual particles in an area A ($\rho = N/A$). In the case of CSR, the expected value of $N(r)$ is $\rho \pi r^2$ at any distance r, thus $K(r)$ equals πr^2. We calculated $K(r)$ using an approximately unbiased estimator as suggested by Ripley (1977, 1979):

$$K(r) = N^2 A \sum_{i=1}^{N} \sum_{j=1, j\neq i}^{N} w_{ij} k(i,j)$$

If the distance between the two particles i and j is smaller than r, then the counter variable $k(i,j) = 1$, otherwise it is zero. The weighting factor w_{ij} for border correction is 1/(fraction of the circumference of a circle centered in i and passing through j that lies within the analyzed area), yielding values between 1 and 4. Calculation of $k(i,j)$ and w_{ij} from the particles' coordinates x and y follows from

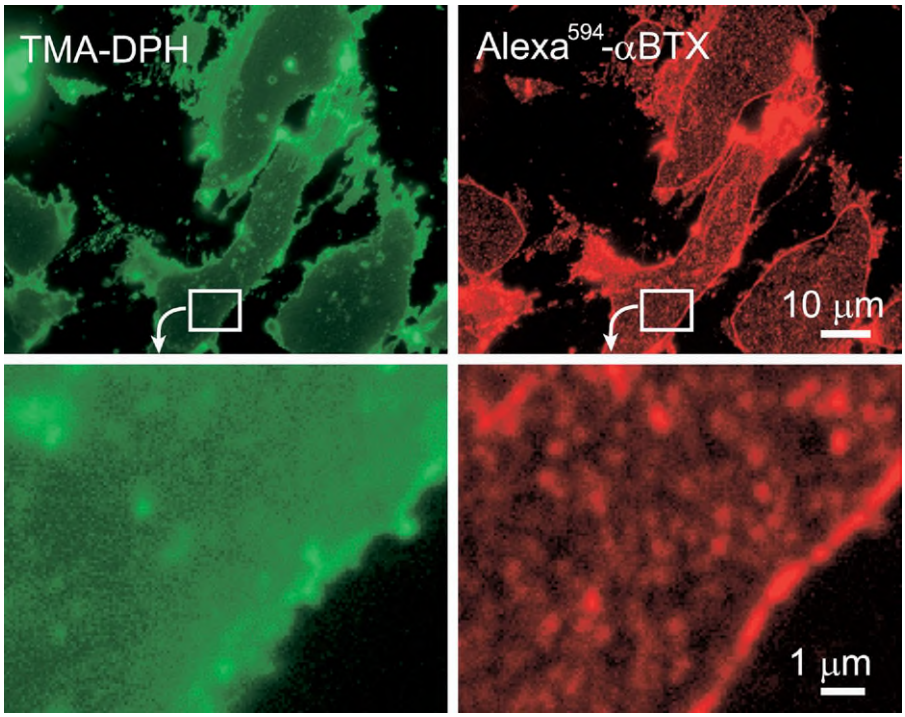

Fig. 1. Wide-field fluorescence images of single membrane sheets obtained from CHO-K1/A5 cells. Single plasma membrane sheets were obtained by ultrasound treatment as indicated in Experimental Procedures, stained with the fluorescent cholinergic antagonist Alexa^{594}-□BTX, and examined by conventional epifluorescence wide-field microscopy; lower panels are zoomed-in subfields from their upper counterparts.

elementary trigonometry. For interpretation using the transformation $L(r)=\sqrt{K(r)/\square}$ and calculating $L(r)-r$ is preferred, since $L(r)-r=0$ for random patterns.

The coordinates of the particles were extracted from the images by determining each particle's center of mass using custom-written software. The upper and lower value of the 99% confidence interval (CI) were estimated by means of Monte Carlo simulations, where for each image the $K(r)$ function for 99 random patterns of same size and particle density was calculated. To allow averaging of data from different images, the estimated 99% CI values were used to normalize each $L(r)$ function for each image. Hence the 99% CI is shown as ± 1 in the $L(r)-r$ plots.

RESULTS

Wide-field fluorescence microscopy images were obtained from single membrane sheets prepared by application of short ultrasound pulses to CHO-K1/A5 cells grown on glass coverslips. This procedure results in the "unroofing" of the cell, leaving only the ventral single plasma membrane adhered to the surface of the glass. Single sheets co-stained with the fluorescent probe TMA-DPH and Alexa^{594}-□BTX, a quasi-irreversible competitive AChR antagonist, are shown in Fig. 1. TMA-DPH is a general lipid fluorescent probe which enables visualization and focusing of thin, two-dimensional specimens, i.e. the isolated plasmalemma. TMA-DPH fluorescence produces a featureless stain depicting the profiles of a few cell membranes adhered to the glass surface. The corresponding Alexa^{594}-□BTX images reveal a finely punctuated appearance of sub-micron sized, diffraction-limited spots featuring a FWHM of ~250 nm.

Two experimental conditions were used for imaging whole cells and single plasma membrane sheets in both confocal and STED microscopy modes. First, fixation was followed by labeling (*"fix–label"*), in which whole CHO-K1/A5 cells or membrane sheets obtained using ultrasound pulses, were fixed with 4% paraformaldehyde and then labeled with mAb 210 and Atto 532 labeled secondary antibody, thus avoiding long-range crosslinking of AChRs by the antibodies (Tzartos et al., 1987). Second, the labeling procedure preceded fixation (*"label–fix"*) allowing crosslinkage between neighboring AChRs. Confocal microscopy revealed fluorescently labeled dots at the surface of CHO-K1/A5 cells (Fig. 2A, B) and sheets (Fig. 4A, B) with an appearance similar to those imaged by wide-field epifluorescence in single plasma membrane sheets (Fig. 1). The average FWHM of the measured spots was 199±34 nm and 191±33 nm when the specimens were "fix–label" or "label–fix," respectively (Fig. 3).

Applying the doughnut-shaped de-exciting STED beam (see Suppl. Fig. S1) narrowed the measured spots to a FWHM of 77.1±32.9 nm and 91.3±40.7 nm for the two aforementioned experimental conditions, respectively (Fig. 3). The striking gain in resolution becomes apparent by side-to-side comparison of the high magnification confocal and STED microscope images (Figs. 2B, D and Fig. 4B, D). Since the measured spots represent a convolution of the particles with the finite effective point spread function, the actual protein agglomerations are in fact even smaller. Thus when antibody-

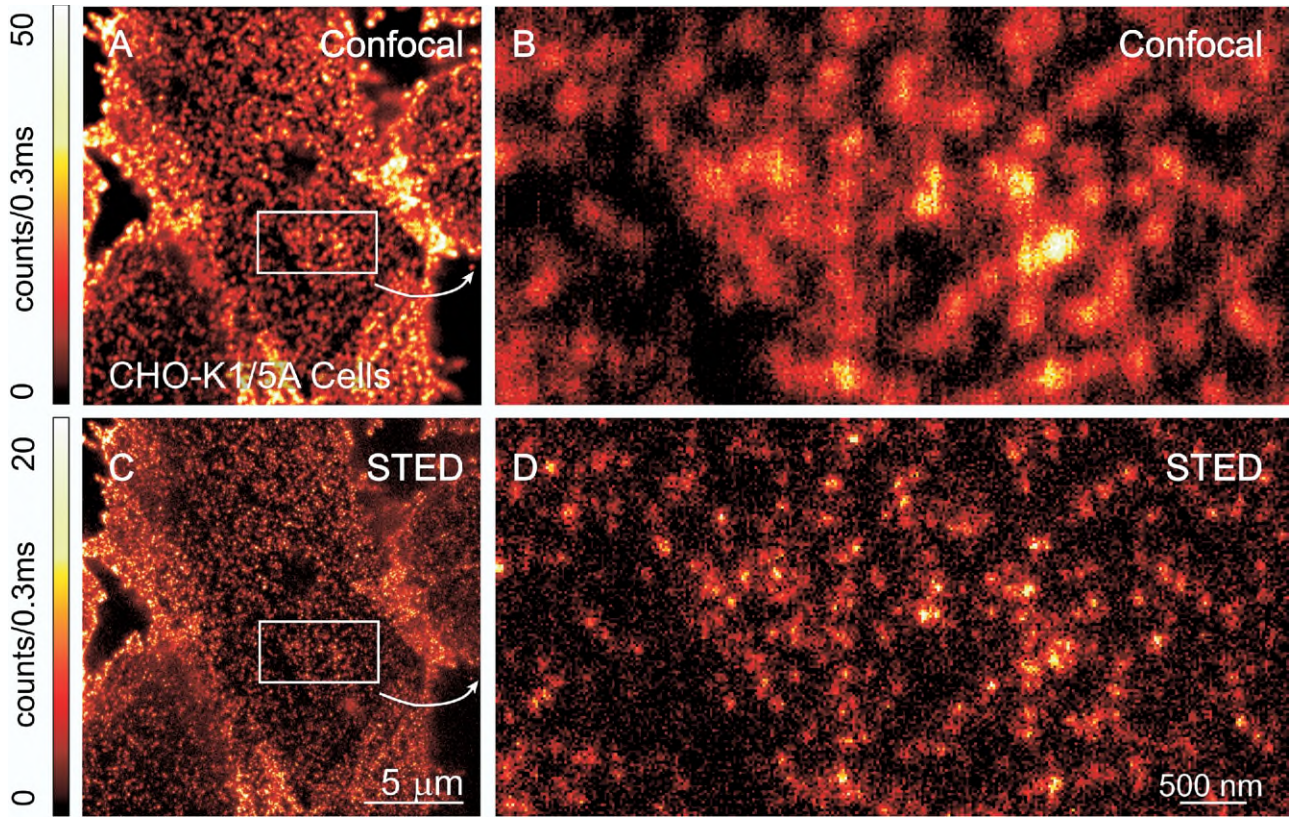

Fig. 2. AChR nanoclusters can be directly imaged on the cell surface of intact CHO-K1/A5 cells. The low magnification 20×20 □m^2 images (A, C) show three different cells that were fixed and then labeled with the mAb210 monoclonal anti-AChR antibody and Atto 532-labeled secondary antibodies. High magnification views of the marked areas provide a side-to-side comparison of the resolution achieved in confocal (B) and STED (D) microscopy. See Figs. 3 and S3 for statistics of size and intensity distribution of the fluorescent AChR spots in confocal microscopy and comparison with the corresponding distributions as observed by STED microscopy.

induced clustering is inhibited by fixation, STED imaging resolves the relatively uniform fluorescent spots delivered by confocal microscopy into smaller AChR particles of variable size, with an estimated average diameter below 55 nm, hereafter referred to as AChR "nanoclusters." This term takes into account the size of fully developed clusters in the adult vertebrate NMJ (reviewed in Willmann and Fuhrer, 2002; Sanes and Lichtman, 2001) or aneural C2 myotubes (23–94 □m in length, Kummer et al., 2004) and the smallest AChR "sub-micron aggregates" visualized by light microscopy in aneural myotubes (Kishi et al., 2005). The histograms depicting the size and intensity distribution of all spots measured are shown in Figs. 3 and S3. Table 1 summarizes the figures.

Comparing the conditions "fix–label" and "label–fix," the small increase in the size distribution of AChR nanoclusters reflects the aggregation induced by the combined effect of primary (anti-AChR) and secondary (IgG) antibodies, a combination that results in patching of cell-surface proteins (Prior et al., 2003) and, in our case, in an increase in nanocluster diameter of ~60% (Table 1). Furthermore, a comparison of the size and intensity distribution of AChR nanoclusters in cells (Fig. 2), and spots in single membrane sheets (Fig. 4), revealed almost no differences for the two conditions tested. This finding indicates that the size distribution of AChR particles in membrane sheets and whole cells is essentially similar (Table 1).

Cholesterol is one of the key lipid components involved in AChR functionality (reviewed in Barrantes, 2003, 2004). Furthermore, cholesterol-enriched membrane domains have been postulated to concentrate signaling molecules and receptors in particular regions of the cell surface (Maxfield, 2002). We therefore performed a series of experiments, asking whether the organization of AChR particles at the cell surface was cholesterol-dependent. Acute CDx treatment is an established procedure to deplete cholesterol from the plasmalemma (see review by Pichler and Riezman, 2004) and to study the effect of cholesterol on the cluster organization of membrane proteins (e.g. Prior et al., 2003). To study the effect of cholesterol depletion from CHO-K1/A5 cells, these cells, or single membrane sheets, were treated with 10 mM CDx at 37 °C for 20 min, labeled with the monoclonal antibody mAb 210, directed against the main immunogenic region of the AChR protein (Tzartos et al., 1987) followed by the Atto 532-labeled secondary antibody, and then fixed (condition "*CDx–label–fix*"). Using this experimental condition in single plasma membrane sheets, epifluorescence wide-field microscopy studies performed in a previous

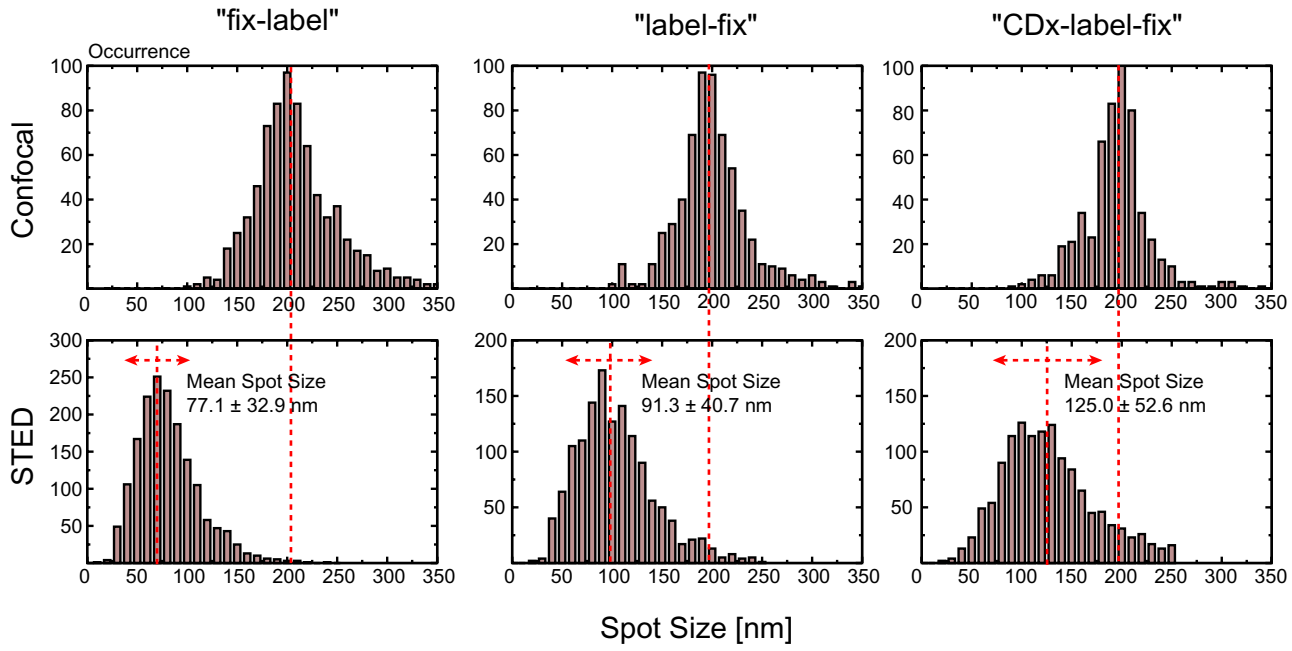

Fig. 3. Size distribution of AChR spots in confocal microscopy and AChR particles in nanoclusters resolved by STED microscopy. The three columns refer to the three experimental conditions tested in this work as indicated and the histograms represent averages of five independent sets of experiments. The total number of particles analyzed is indicated in Table 1. The determinable mean spot size (vertical red lines) is noticeably smaller in the STED images than in the confocal images. Deconvolution of the measured spots with the effective point spread function of the STED mode gives a 99.9% upper limit estimate for the mean AChR particle size of 55 nm (condition "fix–label"), 69 nm (condition "label–fix") and 116 nm (condition "CDx–label–fix").

work revealed an increase in the intensity of the fluorescent spots, which we interpreted as a consequence of the antibody-induced tethering of AChR particles upon CDx treatment (Borroni et al., in press). However, we could not resolve any changes in particle size. Similarly, no statistically significant difference in spot size could be observed between control and CDx-treated samples by confocal microscopy (e.g. Fig. 3). Once again, changes were only apparent in the intensity distribution of the spots which were brighter upon cholesterol depletion (see Table 1 and Suppl. Fig. S3). Whether cholesterol depletion facilitated AChR supramolecular aggregation remained an open question requiring higher spatial resolution to be responded.

As shown in Figs. 5, 3 and Table 1, STED microscopy revealed changes in the distribution of AChR particles upon CDx treatment that were not apparent in confocal microscopy. The analysis of the size and fluorescence intensity distribution of AChR particles in the STED images exhibited a significant broadening of the size distribution. This broadening stems from further aggregation of the small AChR particles, resulting in larger-sized AChR nanoclusters, as detected by STED microscopy, and increased spot intensity as also observed by wide-field (Borroni et al., in press) and confocal microscopies (Fig. S3).

The distribution of AChR clusters in the fluorescence images was also analyzed at larger scales by applying Ripley's K-function (Ripley, 1977, 1979). Representing a second-order analysis of spatial point patterns, the K-function is used to test for spatial randomness. As opposed to nearest neighbor methods, all inter-particle distances over the study area are incorporated into the analysis, thus providing a thorough topographical characterization which in turn is compared with that of a pattern resembling CSR (Ripley, 1977, 1979; see Experimental Procedures and Supplementary data). The data corresponding to whole cells in "label–fix" condition and imaged with STED microscopy showed a random distribution of particles at all length scales (Fig. 6A), i.e. the deviation from the $L(r)-r=0$ curve was within the 99% CI expected for a random distribution. When the same analysis was performed on the membrane sheets (Fig. 6B), the calculated $L(r)-r$ metrics of control plasma membrane sheets and intact cells showed the same tendency.

Depletion of cell-surface cholesterol (Fig. 5) produced a marked alteration of the long-range organization of the AChR in whole cells (Fig. 6A). After cholesterol extraction from the CHO-K1/A5 cells, positive values of the $L(r)-r$ function were observed within a narrow region of the r range analyzed; maximum deviation from the $L(r)-r=0$ curve occurred at radii of ~0.5–1 □m, rapidly falling off to values below the cutoff limit for inter-cluster distances □1.5 □m. Thus cholesterol depletion is accompanied by an increase in long-range interactions (as compared with the nanometer scale of the AChR clusters themselves) and hence a change in AChR cluster distribution made apparent by STED microscopy. The clustering of particles was clearly observed in intact cells but was barely apparent in single membrane sheets, where it could be observed only for length scales between 0.6 and 2 □m (Fig. 6B).

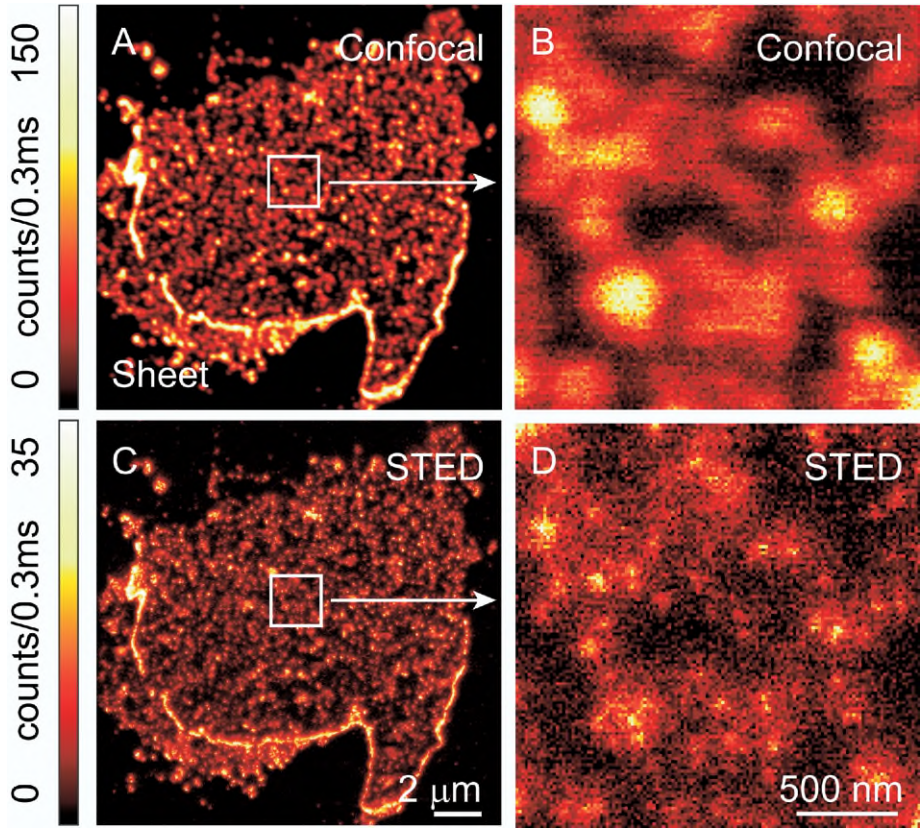

Fig. 4. AChR spots and AChR nanoclusters in single plasma membrane sheets. Plasma membrane sheets were obtained by an ultrasound pulse applied to CHO-K1/A5 cells adhered to the glass coverslip, fixed, labeled and then imaged in the confocal (A, B) and STED (C, D) modes. *Left column*: the entire glass-adhered plasma membrane. *Right column*: high magnification detail of a 1.95×1.95 □m^2 area illustrating the resolution of single confocal spots into multiple AChR nanoclusters with STED microscopy.

DISCUSSION

Using STED microscopy we were able to study changes in the size distribution of AChR nanoclusters well below the diffraction limit of a typical wide-field and a confocal microscope.

The findings of the size distribution analysis indicate that the organization of AChR nanoclusters at the plasma lemma is indeed non-random, as well as cholesterol-dependent at scales below 250 nm. In an elegant recent study using total internal reflection fluorescence (TIRF) microscopy (Demuro and Parker, 2005), AChRs heterologously expressed in oocytes appear to exhibit a random distribution when indirectly imaged by fluorescence changes in Ca^{2+} fluxes. The random, non-clustered distribution of AChRs in the oocyte membrane could be related to the fact that non-aggregating, transiently expressed embryonic-type (□$_2$□□□) AChRs were imaged in the recent Demuro and Parker (2005) study, with a lateral resolution of ~1 □m. By contrast, in our study we

Table 1. Size and fluorescence intensity distribution of AChR nanoaggregates as determined by STED microscopy

Condition	Spot size (nm)		Estimated cluster size (nm)		Intensity (a.u.)	
	Mean	S.D.	Mean	99.9% Upper limit	Mean	S.D.
Whole cells						
"Fix–label"	75.8	32.4	38.8	53.8	347.7	266.5 (n=609)
"Label–fix"	109.7	35.7	92.1	95.3	955.5	868.5 (n=541)
"CDx–label–fix"	120.0	44.74	105.0	110.1	797.3	692.5 (n=734)
Membrane sheets						
"Fix–label"	77.1	32.9	41.1	55.1	323.4	302.5 (n=1075)
"Label–fix"	91.3	40.7	63.3	69.4	442.2	409.4 (n=817)
"CDx–label–fix"	131.1	60.1	118.8	123.1	701.3	874.4 (n=616)

The figure in parentheses (n) indicates the number of AChR particles analyzed in each case. The cluster size was estimated by means of convolution of simulated clusters with the measured point spread function.

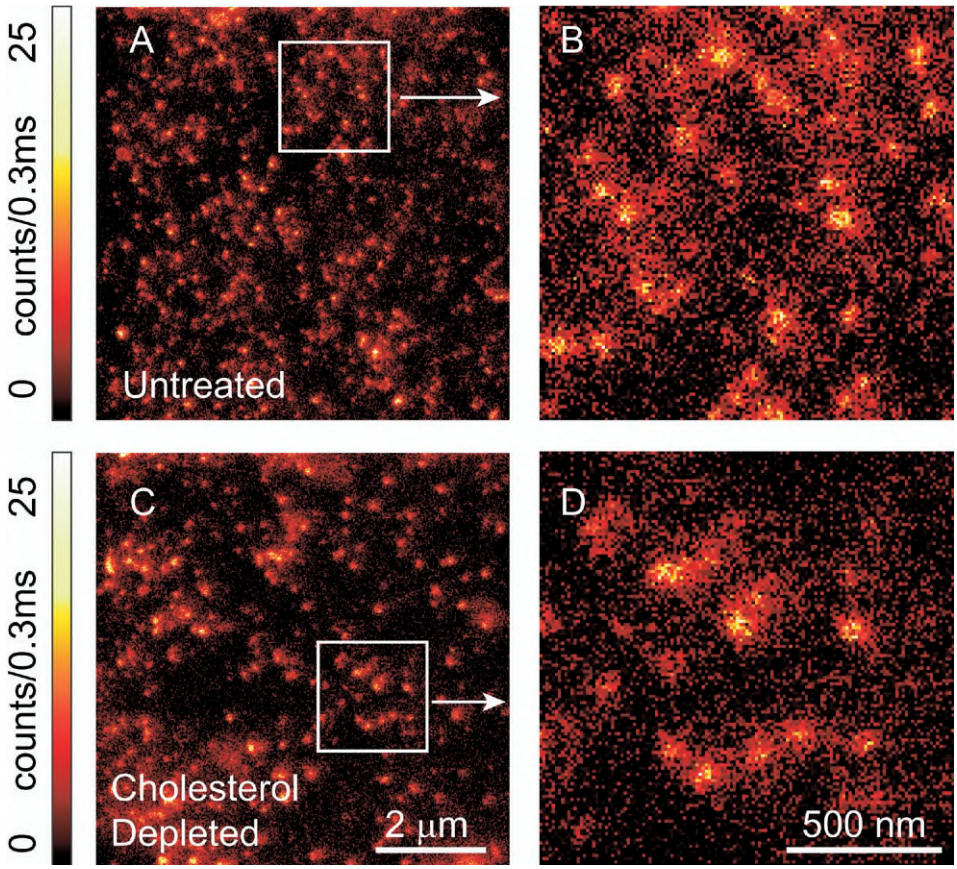

Fig. 5. STED microscopy reveals differences in AChR organization brought about by cholesterol depletion from the plasma membrane. AChR nanoclusters imaged by STED microscopy of single plasma membrane sheets from CHO-K1/A5 cells: A and C show low magnification views, 7.5×7.5 □m^2 in size. Cholesterol depletion (10 mM CDx, 30 min, 37 °C) results in the diminution of the number of AChR nanoclusters (C, D) as compared with controls (A, B). The size distribution also changes, as can be appreciated in the high magnification images (B, D), with a marked tendency toward larger size of AChR nanoclusters upon cholesterol depletion (D). See corresponding histograms in Figs. 3 and S3, and also Table 1.

employ a clonal cell line stably expressing adult-type (□$_2$□□□) AChR, an interesting difference worth addressing in future studies. More likely, however, the disclosure of the clustered supramolecular organization of AChRs in the membrane, and its cholesterol dependence, are a further indication of the ability of STED microscopy to reach hitherto unexplored nanodimensions in biological imaging and provide new information on the supramolecular architecture of the AChR.

The results of the spatial point pattern analysis revealed that the long-range AChR organization at the plasmalemma of CHO-K1/A5 cells depends on cholesterol-sensitive interactions that normally extend over the range of a few microns in untreated cells (<1 □m under our image sampling size, cf. Fig. 6A). A likely candidate for the maintenance of such an influence is the cortical cytoskeleton and, particularly, the actin network (e.g. Kwik et al., 2003). The ability of AChR nanoclusters to aggregate upon cholesterol depletion in whole cells (Fig. 6A) is apparently lost or substantially attenuated in single plasma membrane sheets devoid of the subcortical cytoskeleton (Fig. 6B). This provides additional, albeit indirect, evidence that the long-range AChR supramolecular organization is likely to be associated with the presence of an intact cytoskeletal network under physiological energy supply and normal cholesterol levels (Borroni et al., in press). In muscle, AChRs have been reported to be associated with actin via urotrophin (Willmann and Fuhrer, 2002). The short-range extent and composition of the AChR nanoclusters is probably maintained by protein–protein (i.e. receptor–receptor) and receptor–lipid interactions, of which AChR–cholesterol interactions may constitute the prevailing stabilizing force (Barrantes, 2004).

The present study is the first application of nanoresolving light microscopy to the study of the spatial distribution of an ion channel. Since AChR constitutes the paradigm within the large family of rapid ligand-gated ion channels, the ability to spatially map its supramolecular distribution as well as to determine the size of its nanoaggregates opens new avenues for harnessing the concept of STED fluorescence microscopy to the study of myriad membrane proteins. Moreover, as it is inherently unlimited by diffraction, improvements on the STED technique are likely to increase its usefulness in the neurosciences.

Acknowledgments—This work was partly supported by a joint grant from Fundacion Antorchas (Argentina)/DAAD (Germany) to F.J.B. and S.W.H. F.J.B. acknowledges partial support from CONICET, FONCyT and Univ. Nac. Sur. Thanks are due to Ms Beatriz de los Santos for help in cell culture, to Jan Keller for

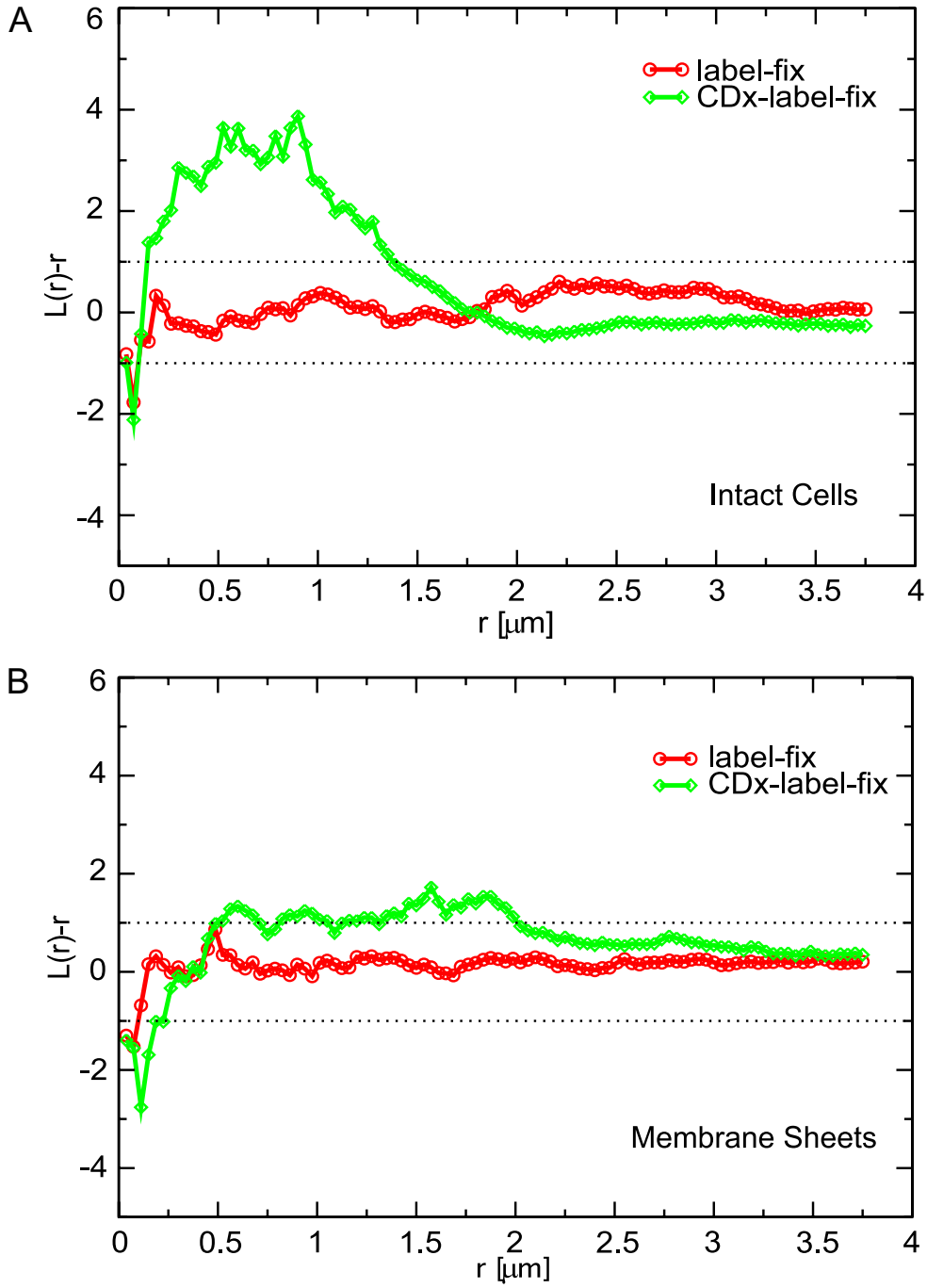

Fig. 6. Statistical evaluation makes apparent changes in long-range AChR nanocluster organization produced by cholesterol depletion of intact cells but not of single plasma membrane sheets. The AChR particle distribution was analyzed using Ripley's K-function (Ripley 1977, 1979). Shown are plots of $L(r)-r$ with 99% CI (dotted lines). Positive values above the 99% CI indicate clustering at the according length scale. (A) Analysis of images corresponding to intact CHO-K1/A5 cells stained with Atto 532 secondary antibodies as shown in Fig. 2. (B) Analysis of images of single plasma membrane sheets obtained by ultrasound treatment of CHO-K1/A5 cells as shown in Fig. 4. The analysis was performed for the conditions "label–fix" and "CDx-label–fix."

doughnut optimizations, and to Andreas Schönle and Volker Westphal for providing software for image analysis.

REFERENCES

Avery J, Ellis DJ, Lang T, Holroyd P, Riedel D, Henderson RM, Edwardson JM, Jahn R (2000) A cell-free system for regulated exocytosis in PC12 cells. J Cell Biol 148:317–324.

Barrantes FJ (2003) Transmembrane modulation of nicotinic acetylcholine receptor function. Curr Opin Drug Disc Dev 6:620–632.

Barrantes FJ (2004) Structural basis for lipid modulation of nicotinic acetylcholine receptor function. Brain Res Brain Res Rev 47: 71–95.

Borroni V, Baier CJ, Lang T, Bonini I, White MW, Garbus I, Barrantes FJ (2006) Cholesterol depletion activates rapid internalization of

diffraction-limited acetylcholine receptor domains at the cell membrane. Mol Membr Biol, in press.
Demuro A, Parker I (2005) "Optical patch-clamping": Single-channel recording by imaging Ca^{2+} flux through individual muscle acetylcholine receptor channels. J Gen Physiol 126:179–192.
Hell SW (1997) Increasing the resolution of far-field fluorescence light microscopy by point-spread-function engineering. In: Topics in fluorescence spectroscopy (Lakowicz JR, ed), pp 361–422. New York: Plenum Press.
Hell SW (2003) Toward fluorescence nanoscopy. Nat Biotechnol 21:1347–1355.
Hell SW (2004) Strategy for far-field optical imaging and writing without diffraction limit. Phys Lett A 326:140–145.
Hell SW, Wichmann J (1994) Breaking the diffraction resolution limit by stimulated emission: stimulated-emission-depletion microscopy. Opt Lett 19:780–782.
Kishi M, Kummer TT, Eglen SJ, Sanes JR (2005) LL5□: a regulator of postsynaptic differentiation identified in a screen for synaptically enriched transcripts at the neuromuscular junction. J Cell Biol 169:355–366.
Klar TA, Jakobs S, Dyba M, Egner A, Hell SW (2000) Fluorescence microscopy with diffraction resolution limit broken by stimulated emission. Proc Natl Acad Sci U S A 97:8206–8210.
Kummer TT, Misgeld T, Lichtman JW, Sanes JR (2004) Nerve-independent formation of a topologically complex postsynaptic apparatus. J Cell Biol 164:1077–1087.
Kwik J, Boyle S, Fooksman D, Margolis L, Sheetz MP, Edidin M (2003) Membrane cholesterol, lateral mobility, and the phosphatidylinositol 4,5-bisphosphate-dependent organization of cell actin. Proc Natl Acad Sci U S A 100:13964–13969.
Maxfield FR (2002) Plasma membrane microdomains. Curr Opin Cell Biol 14:483–487.
Pichler H, Riezman H (2004) Where sterols are required for endocytosis. Biochim Biophys Acta 1666:51–61.
Prior IA, Muncke C, Parton RG, Hancock JF (2003) Direct visualization of Ras in spatially distinct cell surface microdomains. J Cell Biol 160:165–170.
Ripley BD (1977) Modelling spatial patterns. J R Stat Soc B 39: 172–192.
Ripley BD (1979) Tests of randomness for spatial point patterns. J R Stat Soc B 41:368–374.
Roccamo AM, Pediconi MF, Aztiria E, Zanello L, Wolstenholme A, Barrentes FJ (1999) Cells defective in sphingolipids biosynthesis express low amounts of muscle nicotinic acetylcholine receptor. Eur J Neurosci 11:1615–1623.
Sanes JR, Lichtman JW (2001) Induction, assembly, maturation and maintenance of a postsynaptic apparatus. Nat Rev Neurosci 2: 791–805.
Tzartos S, Hochschwender S, Vasquez P, Lindstrom J (1987) Passive transfer of experimental autoimmune myasthenia gravis by monoclonal antibodies to the main immunogenic region of the acetylcholine receptor. J Neuroimmunol 15:185–194.
Willmann R, Fuhrer C (2002) Neuromuscular synaptogenesis: clustering of acetylcholine receptors revisited. Cell Mol Life Sci 59: 1296–1316.

APPENDIX

Supplementary data

Supplementary data associated with this article can be found, in the online version, at doi: 10.1016/j.neuroscience.2006.08.071.